Constrained estimates of externally forced past and future warming in Canada

Tong Li, Francis W. Zwiers, Xuebin Zhang & Xiaolan Wang

2025

Pacific Climate Impacts Consortium (PCIC)

PCIC Publications

Original citation:

Li, T., Zwiers, F. W., Zhang, X., & Wang, X. (2025). Constrained estimates of externally forced past and future warming for Canada. *Earth's Future, 13,* e2025EF006374. https://doi.org/10.1029/2025EF006374

Earth's Future

RESEARCH ARTICLE
10.1029/2025EF006374

Constrained Estimates of Externally Forced Past and Future Warming for Canada

Tong Li[1], **Francis W. Zwiers**[1,2], **Xuebin Zhang**[1], **and Xiaolan Wang**[3]

[1]Pacific Climate Impacts Consortium, University of Victoria, Victoria, BC, Canada, [2]Key Laboratory of Meteorological Disaster, Collaborative Innovation Center on Forecast and Evaluation of Meteorological Disasters, Ministry of Education, Nanjing University of Information Science & Technology, Nanjing, China, [3]Climate Research Division, Environment and Climate Change Canada, Victoria, BC, Canada

Key Points:

- A carefully tested Bayesian constraint is applied to assess both externally forced historical and future warming in Canada
- External forcing from human activity has warmed Canada by 2.2 [1.3, 3.1]°C from the pre-industrial period to the 2015–2024 decade
- The constraint narrows the uncertainty range by 17%–41% by the end of the century

Supporting Information:

Supporting Information may be found in the online version of this article.

Correspondence to:

T. Li,
tongli1997@uvic.ca

Citation:

Li, T., Zwiers, F. W., Zhang, X., & Wang, X. (2025). Constrained estimates of externally forced past and future warming for Canada. *Earth's Future*, *13*, e2025EF006374. https://doi.org/10.1029/2025EF006374

Received 6 APR 2025
Accepted 28 SEP 2025

Author Contributions:

Conceptualization: Tong Li, Francis W. Zwiers, Xuebin Zhang
Data curation: Xiaolan Wang
Formal analysis: Tong Li
Funding acquisition: Francis W. Zwiers
Methodology: Tong Li, Francis W. Zwiers, Xuebin Zhang
Software: Tong Li
Supervision: Francis W. Zwiers
Visualization: Tong Li
Writing – original draft: Tong Li
Writing – review & editing: Tong Li, Francis W. Zwiers, Xuebin Zhang, Xiaolan Wang

Abstract The Arctic has experienced the most rapid warming on Earth in recent decades. This affects Canada's landmass, which extends well into the Arctic. Nevertheless, limited spatial and temporal observational coverage, combined with large climate model uncertainties, pose challenges to understanding both past and future climate changes in these regions relative to preindustrial conditions. This is particularly challenging in a place like Canada that has insufficient historical data to determine preindustrial reference conditions. Emergent constraints can overcome this limitation by using historical observations for the modern post-industrial era to constrain estimates of both preindustrial reference levels and future warming. Here we apply a carefully tested Bayesian observational constraint method to simultaneously assess the externally forced historical and future warming in Canada. Testing indicates that the approach reduces bias and uncertainty in historical and future warming estimates, increasing confidence that it may also serve as a basis for developing a broader understanding of climate change in other high-latitude regions. We estimate that external forcing from human activity, has warmed Canada by 2.2 [1.3, 3.1]°C between the 1850–1900 pre-industrial period and the recent 2015–2024 decade. Applying these same observational constraints to future climate conditions indicates that Canada will warm to 5.1 [3.2, 7.0]°C above pre-industrial levels by the end-of-century under an intermediate emissions scenario SSP 2-4.5, and to 6.7 [4.6, 8.9]°C under a high-emissions scenario SSP 3-7.0, with the largest warming projected for Northern Canada, followed by Quebec.

Plain Language Summary Canada has been warming rapidly, especially in its high latitude northern regions. This study uses a Bayesian observational constraint method to better understand past and future external forced warming for Canada within a consistent framework. This framework, which combines information from climate models and observations, allows us to work backwards in time to estimate the role of external forcing in warming relative to the preindustrial period and forward in time to estimate future mean temperatures. Our findings indicate that Canada experienced minimal warming before the 1930s, with the warming increasing steadily thereafter. External forcing from human activity, especially the emission of greenhouse gases, is estimated to have warmed Canada by 2.2°C from the pre-industrial period to the recent 2015–2024 decade. Future projections depend on the different emissions scenarios, with warming ranging from an estimated 5.1°C under an intermediate emissions scenario SSP2-4.5 to 6.7°C under a high emissions scenario SSP3-7.0 by the end of this century. This study provides a clear understanding of past and future climate change in a region that is strongly affected by feedback processes that amplify warming due to anthropogenic emissions, thereby better informing climate action and policy-making efforts to mitigate the impacts of climate change.

1. Introduction

The global near-surface temperature in 2023 was 1.45°C above the pre-industrial average (WMO, 2023). Warming is occurring at a much higher rate in the northern high latitudes, however, exceeding three times the global average in the Arctic (AMAP, 2021; Rantanen et al., 2022). The warming is accompanied by widespread changes in many other aspects of the physical environment, such as increased precipitation (Min et al., 2008; Zhang et al., 2019), changes in soil moisture (Watts et al., 2025), loss of snow and ice, and thawing of permafrost (Fox-Kemper et al., 2021). These changes have caused damage not only to towns, cities and critical infrastructure but also natural ecosystems (Hjort et al., 2022). Additionally, the thawing of permafrost has resulted in increased releases of greenhouse gases such as methane (Miner et al., 2022).

Understanding the contribution of human activities to past warming since the pre-industrial period 1850–1900 and reliably projecting future warming in high-latitude regions is important not only for local and regional climate adaptation but also for global climate mitigation. Yet, this is challenging due to limited spatial and temporal coverage of past observations. For example, the vast area of Canada north of the 60th parallel has very few observing stations with long-term historical records, that with a few very rare exceptions, only begin after World War II (Vincent & Gullett, 1999; Zhang et al., 2000). Available observations also provide an incomplete picture of Northern Europe and the Arctic Ocean prior to the 1950s. In addition, this challenge is complicated both by the complex feedback mechanisms that amplify warming in high latitude regions and by the large uncertainty in model projected future warming for the region due to differences in the model representation of these processes. As other high-latitude regions, Canada has experienced rapid warming in past decades (Li et al., 2018; Zhang et al., 2019), but consistent estimates of externally forced past and future century-long temperature change are lacking, both for Canada and other high-latitude regions.

Observational constraints are often used to reduce uncertainty in multi-model projections of the climate response to future emissions and have been widely applied at global scales and in various regions (Lee et al., 2021; Li et al., 2024; Liang et al., 2020; Ribes et al., 2021; Shiogama et al., 2022; Tokarska et al., 2020). Climate model estimates of past warming caused by historical emissions are subject to uncertainties that are similar to those affecting projections of future changes for a given scenario (Gillett et al., 2021), such as differences in the climate sensitivities of the models (Sherwood et al., 2020). Therefore, in parallel with constraining future warming using available past observations, it is also beneficial to constrain estimates of human-induced warming relative to the pre-industrial period up to the present day with those observations. This is particularly important for regions with limited long-term observational coverage, such as high-latitude areas (Douville, 2023). We demonstrate that this is possible by treating past attributable warming and future projections consistently within a single Bayesian statistical framework, using available observations to constrain model simulated climate response. Accurately quantifying warming since the preindustrial period at a national and regional scale provides national and regional policy makers with estimates of climate change that align with changes at the global scale that are assessed in IPCC reports and considered in the context of international climate negotiations and agreements like the Paris Agreement (UNFCCC, 2015).

Kriging for Climate Change (KCC), proposed by Ribes et al. (2021), is a Bayesian observational constraint method that integrates historical observations, and simulations of past and future climate change within a unified statistical framework. It explicitly treats missing past and future observations, enabling consistent constraints on both past attributable warming and future climate response. Unlike traditional detection and attribution based approaches (e.g., ASK; Allen and Stott (2003); Stott et al. (2006); Kettleborough et al. (2007)), which rely solely on historical data, or model-weighting and selection methods (e.g., ClimWIP; Knutti et al. (2017); TCRlikely; Cannon (2024)), which often use ad hoc combinations of models and observations, KCC systematically leverages all available data. By making fuller use of observational data and incorporating temporal patterns, KCC has been shown to produce more robust and skillful climate projections than methods based only on recent trends (Li et al., 2025; Ribes et al., 2021). In this work, we develop an implementation of this approach to incorporate not only the time evolution, but also large-scale regional and global-scale information to estimate observationally constrained externally forced past and future warming in Canada and its subregions within a unified framework. The results show that model uncertainty can be substantially reduced in Arctic amplification-affected northern high latitude regions. This work can therefore serve as a foundation for developing a broader understanding of climate change in other high-latitude areas.

2. Materials and Methods

2.1. Data

2.1.1. Observational Data

We use Canadian gridded surface air temperature data (CanGridT mlyV3.1), updated to 2023 with Canada's third generation homogenized station temperature records (Vincent et al., 2020). The updated data set provides monthly mean gridded temperature, with a 10 km spatial resolution across Canada. While an extended version of the data set has full spatial coverage for Canada for the period 1900 to 2023, we use 1948–2023 as observations to constrain model simulated responses because the station data from which the data set is produced are extremely limited in Canada's north prior to 1948. These monthly data are first averaged to annual values, and annual

temperature anomalies are calculated relative to the 1961–1990 baseline. These anomalies are subsequently area-weighted and averaged over Canada and its six subregions defined in the Canada's Changing Climate Report 2019 (Bush & Lemmen, 2019) for the following analyses. Figure S1 in Supporting Information S1 shows the full names and geographic boundaries of the six subregions. Spatially averaged annual mean temperature anomalies for Canada and each subregion are used for subsequent analyses.

The HadCRUT.5.0.2.0 data set is used to estimate the annual global mean surface temperature over the 1948–2023 period (Morice et al., 2021a) and to quantify measurement uncertainty at both the global and regional scales. The observational constraint method used in this study (KCC, Ribes et al. (2021)), which will be described in more detail below, accounts for measurement error in the observations. Measurement uncertainty here refers to all uncertainties that affect the estimation of the annual mean temperature anomalies in a region, which includes instrumental error and sampling errors that affect data homogenization and gridding procedures. HadCRUT5 includes 200 realizations of estimated monthly grid-box average temperatures where differences between realizations reflect uncertainties that arise from measurement error at stations and in the gridding process equally. When computing regional averages across Canada using the HadCRUT5 data set, we first remap the monthly values of HadCRUT5, which are on a $5° \times 5°$ latitude-longitude grid, onto the 10 km CanGridT grid using a nearest-neighbor approach. The remapped data is then used to compute regional mean values from annual averages obtained from monthly values.

2.1.2. Model Data

We use annual mean near-surface air temperature computed from monthly values simulated by an ensemble of climate models participating in the Coupled Model Intercomparison Project Phase 6 (CMIP6, Table S1 in Supporting Information S1) (Eyring et al., 2016b) in four key ways:

1. *Historical warming attribution:* The historical all forcing (hist-ALL) simulations from 25 models participating in CMIP6 are used to establish emergent constraint relationships for estimating observationally constrained responses to all forcings (ALL) (Table S1 in Supporting Information S1). Only the first run of each model is used to keep the influence of internal variability from each model comparable. To estimate observationally constrained responses to natural forcing (NAT), anthropogenic forcing (ANT), greenhouse gas forcing (GHG) and anthropogenic forcing other than greenhouse gases (OA), we use historical all forcing (hist-ALL), natural forcing (hist-NAT) and greenhouse gas forcing (hist-GHG) simulations from 10 climate models participating in the Detection and Attribution Model Intercomparison Project (DAMIP; Gillett et al., 2016) of CMIP6 (Table S1 in Supporting Information S1). Assuming that climate responses to individual forcings are additive (Min et al., 2013; Ribes et al., 2021), we derive responses to ANT as $\mathbf{X}_{\text{ant}} = \mathbf{X}_{\text{ALL}} - \mathbf{X}_{\text{nat}}$ and that to OA as $\mathbf{X}_{\text{oa}} = \mathbf{X}_{\text{ant}} - \mathbf{X}_{\text{ghg}}$. Because the historical simulations often end before the final year of the period used in attribution analyses, they are extended as detailed in Section 2.4 below.
2. *Future projection:* We use historical all forcing (hist-ALL) simulations and future projections under four Shared Socioeconomic Pathways (SSP) emissions scenarios: SSP1-2.6, SSP2-4.5, SSP3-7.0, and SSP5-8.5 simulations from 25 models participating in CMIP6 to establish emergent constraint relationships and obtain observationally constrained future projections. Only the first run of each model is used for the constraint to keep the influence of internal variability from each model comparable.
3. *Internal variability in the observations:* Internal variability in historical observations is estimated using simulations from five large ensembles (bold entries in Table S1 in Supporting Information S1) conducted with ACCESS-ESM1-5 (40 members, Ziehn et al. (2020)), CanESM5 (50 members, Swart et al. (2019)), MIROC-ES2L (30 members, Hajima et al. (2020)), MIROC6 (50 members, Shiogama et al. (2023)) and MPI-ESM1-2-LR (50 members, Gutjahr et al. (2019)).
4. *Effectiveness of the constraining method:* We evaluate the skill of the constrained projections using an imperfect model testing procedure (see Section 2.3 for details). This procedure requires historical simulations that provide pseudo-observations for constraining projections and corresponding future simulations that provide future pseudo-observations that can be compared with constrained projections to verify performance. Models used as pseudo-observations are not used to develop constraints. We select models with at least three runs (Table S1 in Supporting Information S1, entries in italics) for the historical period and for each of the future scenarios. Three runs from each model are used as pseudo-observations to ensure equal contributions from each model and to obtain information about the potential impact of internal variability on constraint effectiveness.

As the model simulations are provided on different native model grids, their annual mean temperatures are remapped onto the 10 km grid using a nearest-neighbor approach. The remapped data are masked to match the availability of the observational data and used to compute regional area-weighted mean values following the same procedure applied to CanGridT data. CanGridT values in coastal regions are derived from land-based stations. It should be noted however, that model values from model ocean grid boxes may be included when model output is remapped onto the CanGridT grid.

2.2. Constraint Method

We use a novel implementation of the Kriging for Climate Change (KCC) observational constraint method (Ribes et al. (2021) in this study. This method has its roots in Bayesian statistics and treats the constraint problem as a missing data imputation problem. It establishes a prior distribution on the relationship between historical and future temperatures in models and then uses observations during periods when both observations and models are available to obtain a posterior distribution on future temperatures that is conditional on the historical observations. This allows for the estimation (i.e., imputation) of missing past and future observations, thereby constraining and updating model behavior.

The statistical model underpinning KCC, described as Eq. 1 in Ribes et al. (2021), can be rewritten as follows:

$$\text{Observations: } \mathbf{Y_o} = H\boldsymbol{Y} + \boldsymbol{\varepsilon}_o, \qquad \boldsymbol{\varepsilon}_o \sim N(0, \boldsymbol{\Sigma}_o) \tag{1}$$

$$\text{Model realizations: } \mathbf{X_i} = \boldsymbol{\mu} + \boldsymbol{\varepsilon}_{x,i}, \quad \boldsymbol{\varepsilon}_{x,i} \sim N(0, \boldsymbol{\Sigma}_x) \tag{2}$$

$$\text{Indistinguishability assumption: } \boldsymbol{Y} \sim \mathbf{X_i} \sim N(\boldsymbol{\mu}, \boldsymbol{\Sigma}_x) \tag{3}$$

In the observations Equation 1, $\mathbf{Y_o}$ is the time series of observations used to constrain model responses and $\boldsymbol{Y}$ is the response to forcing over the entire period of interest. Matrix H is an operator matrix $\begin{bmatrix}\mathbf{I}_h & \mathbf{0}\end{bmatrix}$ that extracts the components of $\boldsymbol{Y}$ that correspond to the period covered by $\mathbf{Y_o}$. Vector $\boldsymbol{\varepsilon}_o$ in Equation 1 represents noise in the observations, associated with internal variability and measurement errors (e.g., sampling uncertainty). This noise is assumed to follow a Gaussian distribution $\boldsymbol{\varepsilon}_o \sim N(0, \boldsymbol{\Sigma}_o)$.

Similarly, in the model realizations Equation 2, $\mathbf{X_i}$ contains a simulated time series produced with one of m models i, $i = 1, \ldots, m$, $\boldsymbol{\mu}$ is the mean over models, and $\boldsymbol{\varepsilon}_{x,i}$ represents the difference between models. This model realization noise is also assumed to follow a Gaussian distribution $\boldsymbol{\varepsilon}_{x,i} \sim N(0, \boldsymbol{\Sigma}_x)$. In contrast with Equation 1, the equation describing model realizations does not include the operator matrix H because the model simulations are complete for the entire 1850–2100 period of interest. The model-observation indistinguishability assumption, shown in Equation 3, serves as a bridge between the observational and model worlds. This assumption states that the forced response in observation $\mathbf{Y}$ is drawn from the same distribution as the model responses $\mathbf{X_i}$.

With the formulation and assumption above, the multivariate Gaussian distribution $\mathbf{Y} \sim \mathbf{X_i} \sim N(\boldsymbol{\mu}, \boldsymbol{\Sigma}_x)$ can be viewed as a prior distribution on possible 1850–2100 forced response realizations of the observed climate, of which only $\mathbf{Y_o} = H\mathbf{Y}$ has been observed for the 1948–2023 period with error. Following Bayes theorem, it can be shown (Ribes et al., 2021) that the posterior (i.e., constrained) distribution for $\mathbf{Y}$ after updating the prior with the observations $\mathbf{Y_o}$ is multivariate Gaussian with mean vector $\boldsymbol{\mu}_{\mathbf{Y}|\mathbf{Y_o}}$ and variance-covariance matrix $\boldsymbol{\Sigma}_{\mathbf{Y}|\mathbf{Y_o}}$ given by

$$\boldsymbol{\mu}_{\mathbf{Y}|\mathbf{Y_o}} = \boldsymbol{\mu} + \boldsymbol{\Sigma}_x H'(H\boldsymbol{\Sigma}_x H' + \boldsymbol{\Sigma}_o)^{-1}(\mathbf{Y_o} - H\boldsymbol{\mu}) \tag{4}$$

$$\boldsymbol{\Sigma}_{\mathbf{Y}|\mathbf{Y_o}} = \boldsymbol{\Sigma}_x - \boldsymbol{\Sigma}_x H'(H\boldsymbol{\Sigma}_x H' + \boldsymbol{\Sigma}_o)^{-1} H\boldsymbol{\Sigma}_x. \tag{5}$$

This distribution describes the constrained estimates of historical attributed warming and future projected warming and their uncertainties.

We consider three approaches for using observed temperatures to obtain the posterior distribution that are distinguished by how the observational vector $\mathbf{Y_o}$ is configured. The first approach (referred to the CA scheme) uses annual mean temperature averaged over Canada, which results in a vector $\mathbf{Y_o}$ of length 76 (one entry for each year between 1948 and 2023). The second approach (termed the SRA scheme) considers broad spatial variations in temperature within Canada during the historical period by using annual regional mean temperatures over six

subregions instead of only the Canadian annual mean temperatures. This is achieved by concatenating the annual mean temperature time series for the six regions into a single long vector of length 456, with corresponding changes to the dimensions and composition of $\boldsymbol{\mu}, H, \boldsymbol{\Sigma}_o$ and $\boldsymbol{\Sigma}_x$. The third approach (termed the NCG scheme) incorporates annual mean temperature over northern Canada (north of 60°N), Canada, and the globe. Previous studies (Qasmi & Ribes, 2022; Ribes et al., 2022) have demonstrated the added value of including global information when constraining regional warming projections. In addition, the high latitude warming indicator is included in the NCG scheme to help provide an observational constraint on the diverse representations of amplified high-latitude warming in models. To ensure that the global and regional components contribute equally to the estimation, only years after 1948 are used. This results in an observation vector $\mathbf{Y}_o$ of length 228. A detailed description of the implementation of the first approach is provided in Appendix A. Once $\mathbf{Y}_o$ and estimates of $\boldsymbol{\mu}, H, \boldsymbol{\Sigma}_o$ and $\boldsymbol{\Sigma}_x$ have been obtained, the estimated $\boldsymbol{\mu}_{\mathbf{Y}|\mathbf{Y}_o}$ and $\boldsymbol{\Sigma}_{\boldsymbol{\mu}|\mathbf{Y}_o}$ can be easily calculated according to Equations 4 and 5. We then generate 100 random samples representing the warming evolution with time from the posterior distribution for subsequent analysis.

2.3. Imperfect Model Test

As mentioned above, we consider three approaches for using available temperature observations to constrain warming in Canada. The CA scheme should be less influenced by low-frequency internal variability because large-scale modes of variability, such as the Pacific Decadal Oscillation, affect different parts of Canada differently (Vincent et al., 2015). Nationally averaging temperature data filters out some of these effects but does not provide information about regional differences in the influence of external forcing on Canadian temperatures. The SRA scheme is designed to mitigate this issue, although uncertainty is higher because temperatures on smaller scales are influenced more strongly by internal variability. Additionally, using an observational vector with more elements necessitates the estimation of a larger covariance matrices, increasing the potential for estimation errors. The NCG scheme builds on the CA approach by further incorporating high-latitude northern region and larger-scale global mean temperature. Since northern region exhibits a stronger local response to global warming and the GSAT reflects large-scale physical processes, including climate sensitivity, radiative forcing response, and circulation patterns. This combined approach therefore integrates information across different spatial scales and is physically grounded.

We use the imperfect model test to find an optimal KCC implementation, which assumes that strong performance across the available "ensemble of opportunity" is indicative of performance that can be expected when observations provide the constraint. In this procedure, simulations from individual climate models that include both past and future states of the climate serve as pseudo-observations. This allows ECs to be repeatedly applied to different realizations of pseudo-observations for the past, with the resulting constrained projections verified against corresponding future pseudo-observations. We select the simulations from models with at least three runs, using the first three runs if more than three are available, as pseudo-observations to ensure equal contribution from each model. When a simulation is used as pseudo-observations, only simulations from other models are used to obtain the prior distribution on historical and future change in the withheld model.

The evaluation considers absolute bias, uncertainty interval width, and the uncertainty interval coverage rate. The bias is quantified as the absolute difference between the constrained or unconstrained best estimates (mean values) and the mean of the three pseudo-observation runs from the same model. This approach allows comparison with the model's forced response, minimizing the impact of internal variability. The uncertainty interval width is defined as the width of 5–95th percentile uncertainty interval (90% confidence interval) of the constrained or unconstrained distribution. In addition, we compute uncertainty interval coverage rates, representing the percentage of pseudo-observations lying within the 5–95th percentile uncertainty interval to ensure that uncertainty is not underestimated.

Ideally, coverage rate of the uncertainty intervals should be the same as the nominal 90% rate, with lower values indicating underestimated uncertainty and higher values suggesting overestimated uncertainty. Departures from the nominal rate in the imperfect model test may occur for several reasons. A working assumption in developing the prior is that the available CMIP6 "ensemble of opportunity" (Tebaldi & Knutti, 2007) can be considered a representative sample that is drawn from the population of all physically plausible representations of the climate system and that for mean temperature, a multivariate Gaussian distribution can be used to represent that population. This assumption may not be fully satisfied, however, given that the available ensemble includes several

high-sensitivity models (Zeke Hausfather et al., 2022). In addition, to parametrize the prior and posterior distributions it is necessary to use estimates of high-dimensional covariance matrices that are obtained from only a limited number of models, which implies that the uncertainty of those estimates should be considered in the construction of uncertainty intervals. We do this in a two-step process. First, prior and posterior distributions are determined using the estimated covariance matrices. Coverage is then evaluated using the imperfect model test (i.e., leave-one-model out cross validation), and based on this, uncertainty ranges are rescaled to ensure that coverage corresponds to the nominally specified value of 90%. We find that a scaling factor of ∼1.3 is needed to achieve the specified level of coverage for the optimal scheme (amongst the CA, SRA and NCG schemes) for Canadian mean temperature. For simplicity and consistency, this scaling factor is applied uniformly across all emission scenarios and regions.

2.4. Temporal Smoothing of Model Simulated Annual Series

As we are most interested in the temperature responses to anthropogenic forcing both in the past and future, we apply natural cubic spline smoothing to the time series of each simulation to filter out internal variability and short-duration natural forcing effects. Annual mean regional mean series from historical all-forcing simulations (1850–2014) from 25 CMIP6 models are joined with series from corresponding simulations under the SSP1-2.6, SSP2-4.5, SSP3-7.0, and SSP5-8.5 scenarios (2015–2100) to produce continuous annual mean series covering 1850–2100. Additionally, the series extended with the SSP2-4.5 scenario is used to estimate the constrained historical response to ALL forcing. To smooth the annual series, we apply cubic splines with knots placed randomly, ensuring that the spacing between consecutive knots is between 15 and 30 years. To ensure results are not sensitive to a particular knot placement choice, this smoothing process is repeated 10 times with different random knot placements; the mean of the resulting smoothed series is used for subsequent analysis. This approach retains signals only at multi-decadal time scale, approximately 20 years or longer.

The observational data ends in 2023 while the historical simulations provided by the 10 models participating in DAMIP under ALL, NAT, and GHG forcings end in 2014. We therefore need to extend these series so that recent observations can help inform the constraints. Four DAMIP models (CanESM5, IPSL-CM6A-LR, MIROC6, NorESM2-LM) provide ALL, GHG, and NAT forcing simulations under the SSP2-4.5 scenario which we used to extend their historical simulations to 2025. For the remaining DAMIP models, smoothing splines based on 1850–2014 individual forcing simulations developed as above using repeated random knot placement at intervals of 15–30 years were extrapolated for the years 2015–2025. To assess the reliability of this extrapolation, we compare extrapolated with interpolated values for 2015–2025 for the four DAMIP models with complete time series (Figure S2 in Supporting Information S1). The consistency between the two approaches seen in Figure S2 in Supporting Information S1 supports the validity of the extrapolation.

2.5. Estimating Warming Relative to a Base Period and the Instantaneous Warming Rate

We estimate warming relative to two key periods: a modern period that covers the first 30-years of the observational record (1948–1977) and the pre-industrial period (1850–1900). This includes warming in the decade 2015–2024 relative to these two references periods that is attributable to various external forcings, and the projected future warming. Upper and lower bounds of the correspond uncertainty ranges are given by 5th to 95th percentiles that are obtained by sampling from the posterior (observationally constrained) distribution of model simulated warming. Additionally, we calculate instantaneous warming rates for specific years by computing the first derivative of the warming corresponding to that year.

3. Results

3.1. Selecting Optimal Constraining Scheme

Figure 1 illustrates the performance of constrained temperature projections for Canada at the end-of-century 2081–2100 period relative to preindustrial period 1850–1900 under the SSP5-8.5 scenario, using observed temperature with the CA, SRA and NCG schemes, as evaluated through the imperfect model test. The constrained projections from all schemes reduce biases by more than 0.3°C (19%) on average, and the uncertainty interval width is reduced by more than 2°C (31%) relative to the uncertainty of the unconstrained projections, albeit with some reduction in the coverage rate.

10.1029/2025EF006374

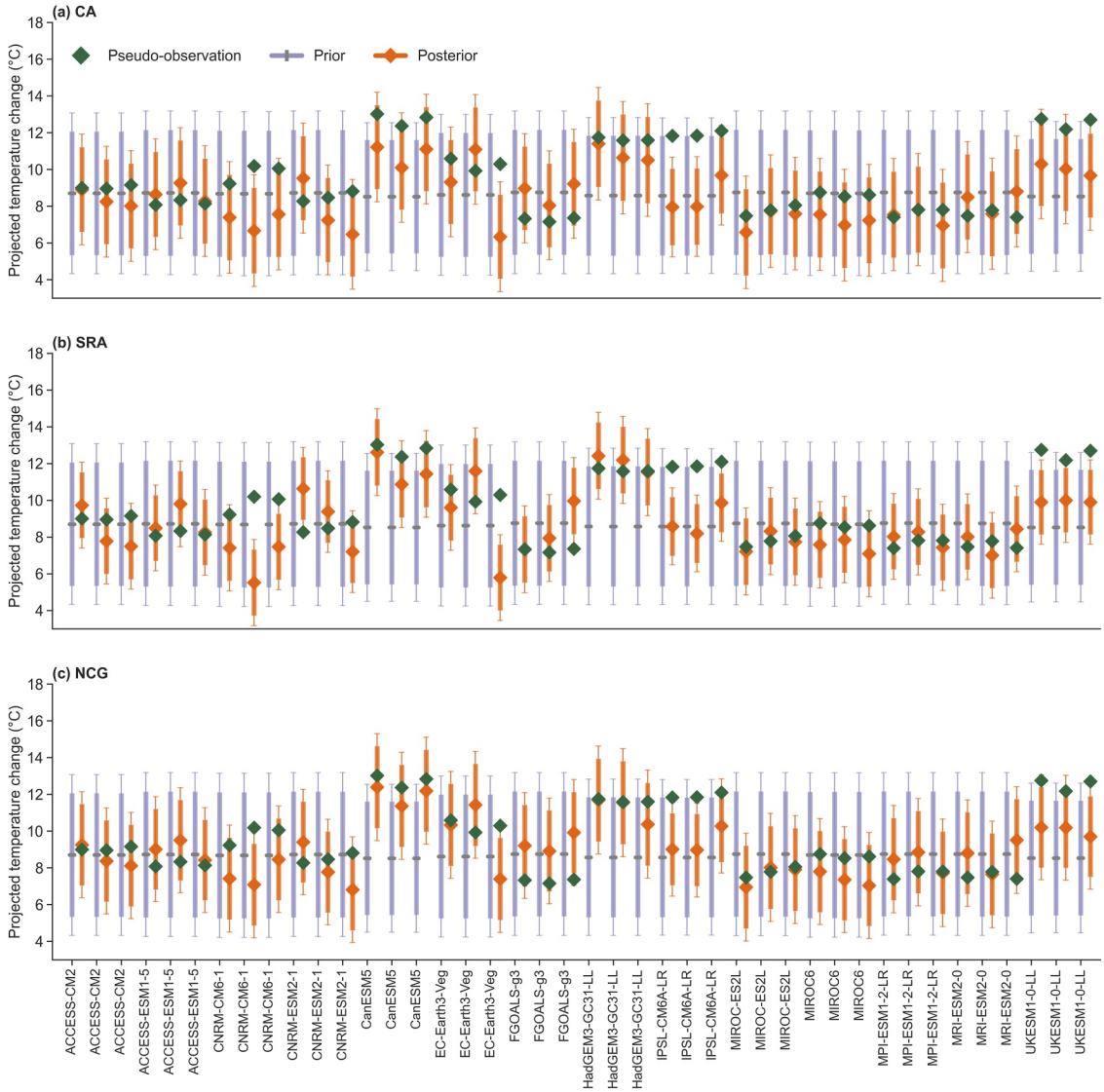

Figure 1. Imperfect model test of constrained projections of Canada's annual mean temperature under the SSP5-8.5 scenario, when each model simulation individually serves as historical and future pseudo-observations. Pseudo-observed changes between end-of-century 2081–2100 and preindustrial period 1850–1900 are represented by dark green markers. The unconstrained distributions, based on simulations by CMIP6 models excluding the model generating the pseudo-observation, are shown as horizontal gray bars (mean values) and wide bars (5th–95th percentiles). The constrained projections, which incorporate historical pseudo-observed information for 1948–2023, are indicated with orange markers and wide bars for the (a) CA, (b) SRA, and (c) NCG schemes respectively. The thin whiskers represent enlarged uncertainty ranges, scaled by a common factor of 1.3 to achieve a 90% coverage rate for the NCG scheme. See Figure S3 in Supporting Information S1 for corresponding results under the SSP2-4.5 scenario.

Among the three constraint schemes evaluated, the NCG approach demonstrates the most balanced performance. It achieves the lowest absolute bias of 1.1°C, representing a 35% reduction compared to unconstrained projections and thus indicating the closest alignment with the pseudo-observations. Its uncertainty width of 4.4°C is narrower than the CA scheme (4.6°C) and while wider than that of SRA (3.6°C), it achieves a coverage rate of 83%, which is higher than the prior (78%) and the constrained CA (78%) and SRA schemes (71%), which implies that its uncertainty estimates are better calibrated to include the true values. In contrast, while the SRA scheme offers the narrowest uncertainty bounds, its lower coverage indicates uncertainty interval width underestimation. The CA scheme, although slightly less accurate and broader in uncertainty, maintains a higher coverage rate. Overall, the NCG schemes appears to offer the best trade-off between bias and uncertainty, making it a compelling choice. Similar performance is observed under the mid-range emissions scenario SSP2-4.5 (Figure S3 in Supporting Information S1).

10.1029/2025EF006374

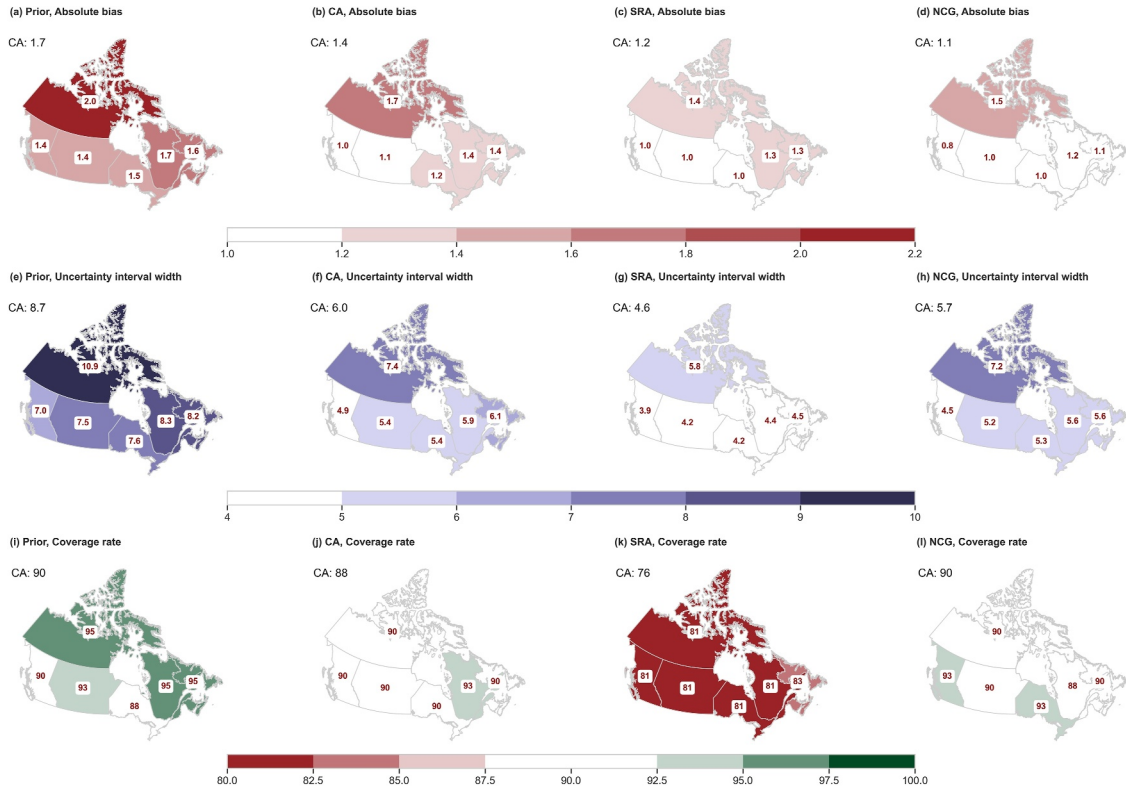

Figure 2. The performance of constrained projections in six sub-regions as determined by the imperfect model test. (a–d) Absolute bias (°C), (e–h) scaled uncertainty interval width (°C) and (i–l) coverage rate (%) in the unconstrained projections (column1), constrained projections using the CA (column 2), SRA (column 3), and NCG (column 4) schemes for 2081–2100 mean conditions relative to 1850–1900 under the SSP5-8.5 scenario. The bias, uncertainty interval width and coverage rate values for each region are indicated within the corresponding regions, with the values for the Canada (CA) region shown in the upper-left corner. See Figure S1 in Supporting Information S1 for the full names and geographic boundaries of the six sub-regions and see Figure S4 in Supporting Information S1 for the results under the SSP2-4.5 scenario.

The fact that all schemes exhibit coverage rates lower than the nominal 90% indicates that the original estimates are likely overconfident. To correct for this, we applied a simple scaling factor of 1.3 to widen the uncertainty ranges, ensuring that the NCG scheme achieves the target 90% coverage rate, while the coverage rates of CA and SRA are 88% and 76% respectively after adjustment under SSP5-8.5. The expanded uncertainty ranges are indicated by the thinner whiskers in Figure 1. Three main factors appear to contribute to the under-coverage. First, imperfect bias correction may be a factor. The projections are constrained by historical information in the pseudo-observations in a limited high-latitude area that is affected by strong positive feedback that amplifies warming. The strength of those feedbacks, which are dominated by ice-albedo feedback, likely depends on more factors than just the amount of warming induced by external forcing. Thus historical data in such areas may not have sufficient information to distinguish amongst potential future evolutions that are, in part, determined by these regional feedback mechanisms. Another factor is internal variability, which despite the size of the Canadian domain, can sometimes be confounded the historical warming signal and lead to divergent projections. For example, this is evident when using EC-Earth3-Veg pseudo-observations (Figure 1), where constrained projections of individual future pseudo-observations show biases that are both positive and substantially negative. Third, model uncertainty (e.g., as characterized by differences in model sensitivities) more generally plays a role.

Focusing on the subregion scale, observationally constrained projections improve upon raw model projections for each of the six subregions (Figure 2), reducing both bias and uncertainty interval width, with the inflated uncertainty range helping to maintain a more reliable coverage rate. Among the three schemes, NCG consistently achieves the lowest absolute biases in southern regions, with only slightly higher bias than SRA in the northern area. Like its performance at the national scale, NCG maintains well-balanced uncertainty widths, narrower than for CA and unconstrained projections and slightly wider than SRA. Importantly, it shows consistently high coverage rates across all regions, ensuring that its uncertainty bounds reliably contain the true values. In contrast,

while SRA offers narrower uncertainty intervals, its lower coverage indicate uncertainty is underestimated (Figure 2k).

The largest absolute reductions in both bias and uncertainty are observed in the northern region, where NCG reduces the bias from 2.0°C in the raw model simulations to 1.5°C and reduces the uncertainty interval width from 10.9°C for to 7.2°C. This highlights the utility of the observational constraint based on 1948–2023 observations in projecting warming in an Arctic region where Arctic amplification and the reduction of Arctic sea ice are important elements contributing to amplified regional warming.

The strong performance of the observational constraints in projecting future climate under the SSP5-8.5 scenario is maintained across other SSP scenarios that have weaker warming signals (evaluations under SSP2-4.5 are shown in Figure S4 in Supporting Information S1). Overall, using observed temperature as a constraint effectively reduces bias and uncertainty in model projections of annual mean temperatures for Canada and its subregions, consistent with similar performance seen at the global scale (Li et al., 2025). Accounting for information from Canada's high-latitude region, its national mean, and the global mean enables the NCG scheme to provide robust and well-calibrated results at both national and regional scales. The remainder of the paper therefore presents attribution results and future projections using this scheme, incorporating the adjusted (scaled) uncertainty ranges.

3.2. Historical Responses to External Forcing

Figure 3a shows observation-constrained estimates of historical responses to external forcing in Canada, with annual values expressed as differences from the 1850–1900 period average constrained value. The constrained ALL forcing response estimate based on 25 CMIP6 models shows a consistent warming trend, beginning near zero during the pre-industrial period (1850–1900), gradually increasing through the early-to-mid 20th century, and accelerating after the 1970s. These two periods of rapid warming align well with global mean surface temperature trends (Fig. 7 in Forster et al. (2025)). The results based on 10 individual climate change simulations participating in DAMIP demonstrate that the attributions to ALL and ANT are very similar (Figure S5 in Supporting Information S1). This trend reflects the growing influence of anthropogenic activities, particularly GHG emissions. The response to OA forcing (mostly from aerosols) exhibits a modest cooling trend that offsets some of the GHG-induced warming and flattens after the 1980s, reflecting stabilization of global OA forcing. The estimated cooling offset from OA is small in Canada, presumably because it does not have many localized aerosol precursor emissions compared to other regions of the world of a similar size, such as south-east Asia. NAT remains nearly flat throughout the historical period and does not make a material contribution to the warming at the response timescales (about 20 years or longer) that are retained in the analysis. Compared to the raw model-simulated responses (Figure S6 in Supporting Information S1), the observation-constrained estimates have tighter uncertainty ranges and reduced warming attributed to ALL, ANT, GHG, and OA.

The observation-constrained temperature responses over Canada and its subregions during the recent decade (2015–2024), expressed as differences from constrained values for 1948–1977, are shown in Figure 3b. We consider a forcing effect to be detected if, after being constrained by observations, its estimated uncertainty range does not include zero. By doing so, we find that warming due to ANT and GHG forcing is detectable in the temperature change between 1948–1977 and 2015–2024 in Canada and all of its subregions. In contrast, the effects of NAT and OA forcing are undetectable in the changes that occurred between these periods. These results are consistent with a previous detection and attribution analysis using an optimal fingerprinting approach (In Bush & Lemmen, 2019; Wan et al., 2018) that detected the effect of ALL and ANT forcing in annual mean temperature in Canada and in 4 subregions covering the country.

The total warming response to ALL forcings in the change in Canada's mean temperature between 1948–1977 and 2015–2024 is estimated at 1.9 [1.6, 2.2]°C. This warming is almost entirely attributed to ANT, contributing 2.1 [1.8, 2.4]°C, possibly offset by a small cooling of −0.1 [−0.3, 0.2]°C due to NAT. The warming from ANT that is driven by GHGs, estimated at 2.3 [1.6, 2.9]°C, is indistinguishable in Canada from that due to GHGs as that from OA, which is estimated to be −0.0 [−0.8, 0.7]°C. Attributable warming across subregions is of similar magnitude, except for the Northern region, where the warming attributed to ALL forcing is 2.3 [1.9, 2.6]°C.

The observation-constrained estimates of temperature change for 2015–2024 relative to the pre-industrial period are shown in Fig. S7 in Supporting Information S1. The detection results for changes relative to the pre-industrial period in Canada and across six subregions are similar to those relative to 1948–1977; the effect of ANT and GHG

10.1029/2025EF006374

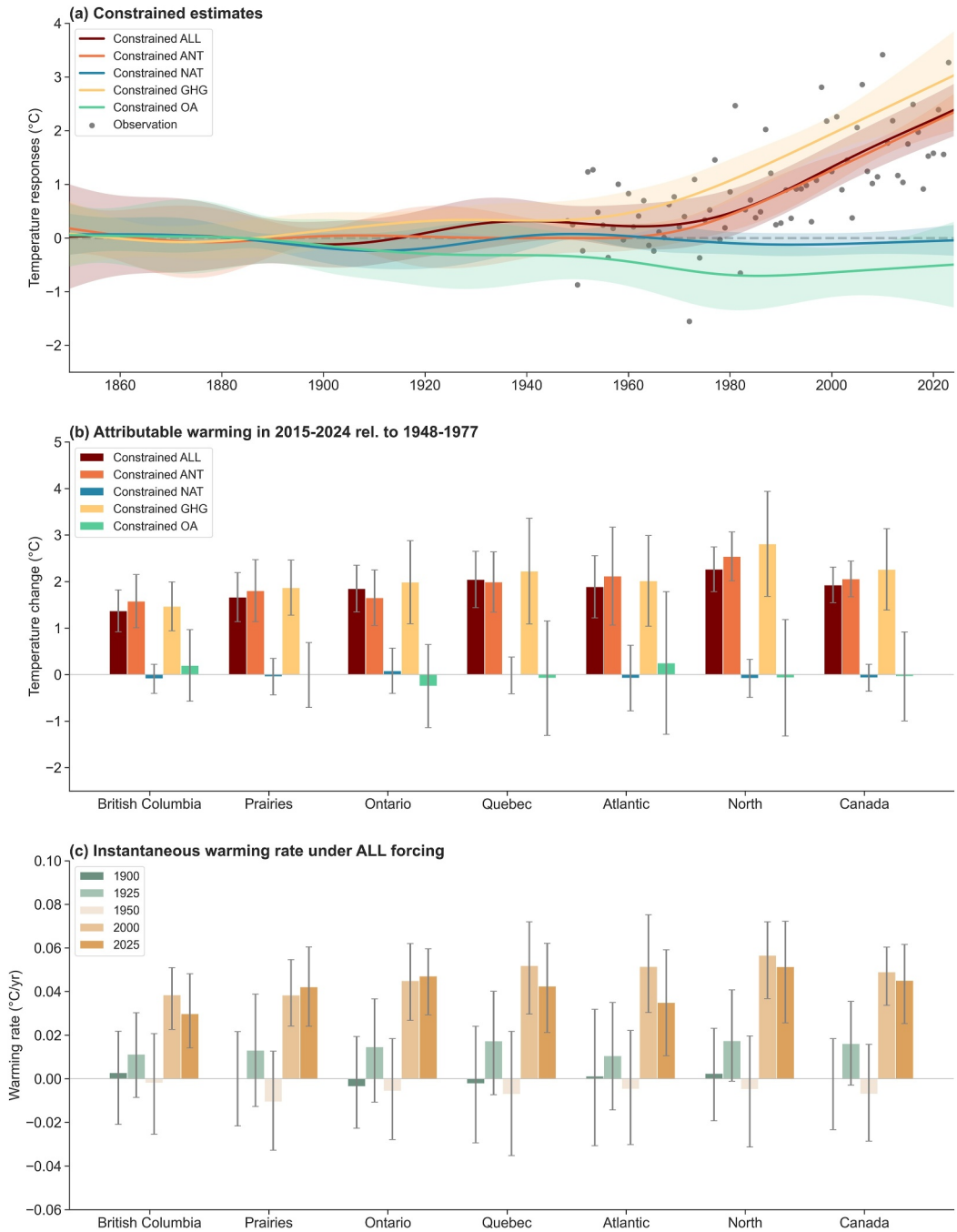

Figure 3.

can be detected in Canada and all of its subregions, and NAT and OA are undetectable in most cases. Warming in Canada between 1850–1900 and 2015–2024 that is attributable to ALL forcing reaches 2.2 [1.3, 3.1]°C, which is about 0.3°C greater than the warming due to ALL forcing since 1948–1977. The uncertainty range in the ALL forced warming over the longer period is 1.2°C wider than for the more recent interval, reflecting the greater uncertainty that arises when referencing changes to constrained estimates of pre-industrial temperatures when observations were not available. Nevertheless, the fact that the historical observations since 1948 provide useful information to meaningfully constrain the ALL forcing change in Canada since the pre-industrial period is remarkable. The estimated warming due to ALL forcing is primarily driven by human activities. The effect of NAT forcing remains minimal at −0.1 [−0.3, 0.2]°C. In contrast, the GHG forcing is estimated to have caused a warming of 2.8 [2.0, 3.7]°C, which over the longer period, has been offset by a cooling induced by OA forcing of −0.5 [−1.3, 0.2]°C. The proportion of GHG-induced warming relative to pre-industrial levels that is offset by OA cooling is larger than that relative to 1948–1977, highlighting the impact of higher aerosol forcing before the 1970s.

Figure 3c displays warming rates in response to ALL forcing at five specific times between 1900 and 2025. Across all regions and in Canada, the warming rate is small in the early 20th century and attains high levels in the early 21st century. By 2025, the warming rate for Canada is approximately 0.045 [0.025, 0.062]°C per year. Regionally, the strongest warming rates are observed in the North, exceeding 0.05°C per year. The spatial and temporal patterns and magnitudes of warming under ANT forcings (Figure S8a in Supporting Information S1) resemble those under ALL forcings, with larger warming rates in the early 21st century, again indicating that the observed warming trend is predominantly human-driven. The constituent GHG forcing of ANT appears to be the dominant driver of these warming trends, with GHG-induced rates (Figure S8b in Supporting Information S1) closely aligning with those of ANT forcings but showing slightly higher magnitudes.

3.3. Future Warming Projection

Constraining future projections with the 1948–2023 observations has two effects on the raw model projections: the distribution of projections is generally adjusted downward and the associated uncertainty is reduced (Figure 4). This pattern is evident for Canada as whole (Figures 4a–4d), and for all six subregions (Figures 4g and 4h). Across all regions and scenarios, the constraint narrows uncertainty range by 17%–42% by the end of the century, these reductions become more even pronounced under the higher-emissions scenarios SSP3-7.0 and SSP5-8.5. The northern region shows highest warming magnitude, with the largest uncertainty reduction, which decreases by 2.5°C (40%) under the SSP2-4.5 scenario. Compared to western Canada, the adjustments in both the mean values and uncertainty are more noticeable in eastern Canada. These constrained reductions in high-end projections, particularly under high emission scenarios and in the northern region, are consistent with findings from Cannon (2024).

Tables S2 and S3 in Supporting Information S1 summarize the magnitude of warming for each region in the near-term (2026–2046) and the late 21st century (2081–2100) under different emissions scenarios, relative to the modern period (1948–1977) and the pre-industrial period (1850–1900), respectively. Under the moderately low emissions scenario SSP2-4.5, which more closely aligns with future mitigation policies, the projected warming for Canada relative to 1850–1900 reaches 5.1 [3.2, 7.0]°C by the end of the century and rises to 6.7 [4.6, 8.9]°C

Figure 3. Observationally constrained estimates of changes in annual mean temperature in Canada. (a) Constrained estimates of Canada's annual mean temperature responses to all forcing (ALL), anthropogenic forcing (ANT), natural forcing (NAT), greenhouse gas forcing (GHG), and other anthropogenic forcing (dominated by aerosols, OA). Temperature responses to various forcings, along with their 5%–95% uncertainty ranges, are shown in color, while observations are plotted as gray dots. The response to ALL forcing is based on simulations from 25 CMIP6 models, while responses to individual forcings are derived from simulations by 10 models participating in DAMIP. Observed and constrained temperatures in this figure are given as differences from the 1850–1900 mean. The best estimate and associated uncertainty of the constrained estimations are initially calculated relative to 1850–2023, then shifted to be relative to 1850–1900 according to mean change. This prevents artificially narrow uncertainty ranges during the reference period, which would otherwise increase as the temporal distance from the reference period grows. The observed annual mean temperatures used with the KCC method were calculated relative to the 1961–1990 mean but are offset in this figure for display purposes. This offset ensures that the observed annual temperatures between 1948 and 2023 have the same mean as the constrained ALL forcings annual temperature estimates for that period. See also Figure S6 in Supporting Information S1 for the projections from unconstrained simulations. (b) Estimated temperature changes due to various external forcings during the past decade 2015–2024 relative to the 1948–1977 period for annual mean temperature in Canada and its six sub-regions (°C). The 5%–95% uncertainty ranges are derived by calculating the difference between the two periods repeated for each sample in the posterior distribution. Results for temperature changes relative to the pre-industrial baseline are provided in Figure S7 in Supporting Information S1. (c) Instantaneous warming rate at various time points in response to ALL forcing for annual mean temperature in Canada and its six sub-regions (°C/yr). See also Figure S8 in Supporting Information S1 for instantaneous warming rate under ANT and GHG forcings.

10.1029/2025EF006374

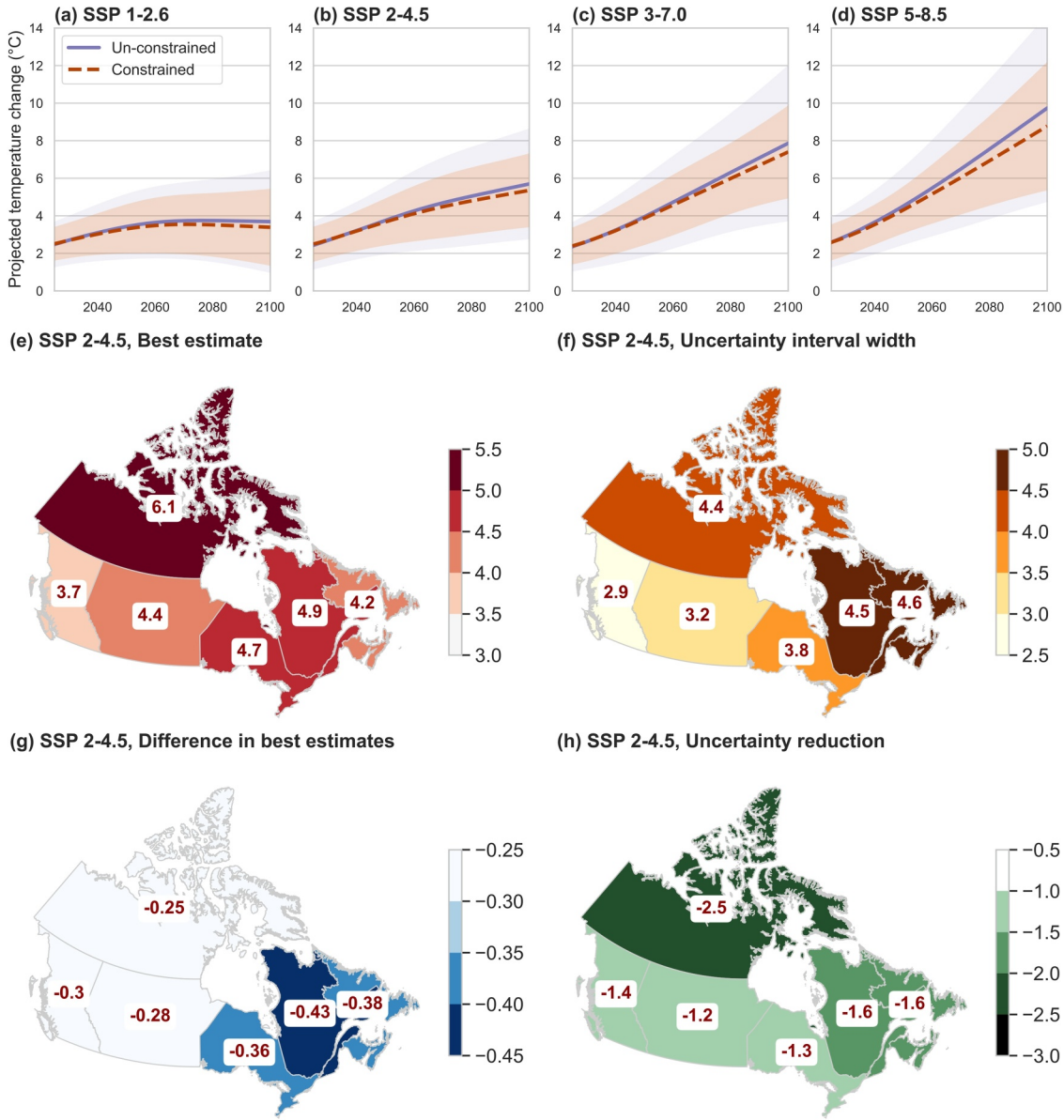

Figure 4. Observationally constrained projections. (a–d) Constrained projection of Canada's annual mean temperature change during 2026–2100, relative to the pre-industrial (1850–1900) baseline, under the four illustrative SSP scenarios considered in this study. The best estimates and their 5%–95% uncertainty ranges of the unconstrained (i.e., raw model projection, light purple) and constrained (orange) projections are shown. (e) Best estimate of the constrained projection for sub-regions at the end of the 21st century (2081–2100) under the SSP2-4.5 scenario. (f) 5%–95% uncertainty range in the constrained projection. (g) Difference between the best estimates of the constrained and unconstrained projections. (h) Reduction in the width of the 5%–95% uncertainty ranges between the constrained and unconstrained projections. Temperature unit is °C. See also Figure S9 in Supporting Information S1 for the projection under the SSP3-7.0 scenario.

under the higher emissions SSP3-7.0 scenario. The largest projected warming under SSP2-4.5 is seen in northern Canada at 6.1 [3.9, 8.3]°C (Figure 4e), and eastern Canada is expected to experience greater warming compared to central and western Canada, where diminishing sea ice and changes in snow cover are likely contributing to a higher warming rate (Screen & Simmonds, 2010; Vihma, 2014).

Projections under different emissions scenarios (Figures S9 and S10 and Tables S2 and S3 in Supporting Information S1) are similar in the near term but diverge more widely by the end of the 21st century. While warming rates remain relatively similar in the near term (e.g., 2026), differences begin to emerge in the following first half of the century (e.g., 2050) and become pronounced by the end-of-century (e.g., 2090) (Figure S10 in Supporting Information S1). Under the SSP1-2.6 scenario, the warming rate slows to nearly zero and even shows small

decline (with high uncertainty) in the latter half of the century. In contrast, the warming rate under a higher emissions scenario SSP5-8.5 remains nearly constant throughout the century, with the warming rate for Canada projected to rise to about 0.09°C per year by the end of century—about double the current rate. The difference in warming rates between SSP5-8.5 and SSP2-4.5 is around 0.06°C per year, highlighting the urgent need for robust mitigation actions to limit the ever-increasing impacts of climate change. In northern Canada, scenario differences are even more pronounced. The warming rate is projected to be about 0.03°C per year under SSP2-4.5, increasing sharply to 0.11°C per year under SSP5-8.5. This illustrates not only the region's heightened sensitivity to global emissions but also the influence of Arctic local feedbacks such as ice-albedo feedback that contribute to a more complex and accelerated warming pattern in the North (Dai et al., 2019; Pithan & Mauritsen, 2014).

4. Discussion and Conclusions

The goal of this study is to attribute past changes and to project the future state of Canada's temperature at both national and subregional scales, while minimizing uncertainty in the estimates. Achieving this objective is challenging because nation-wide observations are not extensively available prior to the late 1940s, and because of the heightened uncertainty in Canadian temperature changes in model simulations compared to most other regions, partly due to Arctic amplification. To address these challenges, we integrate data from existing observations and simulations available from the CMIP6 project using a Bayesian-based observational constraint method. Our approach uses the same observational data and statistical tools to constrain both historical temperature changes attributable to external forcings and projections of future temperature. This consistency allows us to treat attribution and projection as interconnected problems. As other high-latitude regions face similar challenges in understanding the past and projecting the future, the constrained results gained here also demonstrates how we can enhance our understanding of climate change in these regions. Confidence in our results is strengthened by an imperfect model test that helps ensure robustness and to avoid overly confident uncertainty estimates.

We observed that Canada experienced minimal warming during the pre-industrial period, shifting to rapid warming after the 1970s. The warming rate has increased steadily over past seven decades, reaching 0.045°C per year for Canada by 2025, with the northern regions exhibiting the highest rate, exceeding 0.05°C per year. Extending the analysis back to the pre-industrial period, the warming in the recent decade (2015–2024) across Canada reaches 2.2°C, which is primarily from greenhouse gas (GHG) forcing (2.8°C). Warming attributed to anthropogenic (ANT) forcing and GHGs is detectable in all subregions, while contributions from other anthropogenic (OA) and natural (NAT) forcing remains undetectable in most areas.

Compared to raw model outputs, the constrained projections show lower mean warming across all regions under all scenarios together with reduced uncertainty, resulting in a substantial reduction in the 95th percentile of projected warming amounts. The constraint narrows the uncertainty range (5th to 95th percentile) by 17%–42% across all subregions by the end of the century. Constrained future projections suggest a warming of 5.1 [3.2, 7.0]°C in Canada relative to the pre-industrial period by the end of the century under the intermediate SSP2-4.5 scenario, and 6.7 [4.6, 8.9]°C under the higher emissions scenario SSP3-7.0. The large variation of projections under different emissions scenarios underscores the critical need for climate action. Regionally, Northern Canada is projected to experience the largest warming, reaching 6.1 [3.9, 8.3]°C under SSP2-4.5, and eastern Canada is generally expected to warm more than western Canada.

Compared to previous work by Ribes et al. (2021) and Li et al. (2025), we refined the implementation of time series smoothing to better extract the forced responses from models. Ribes et al. (2021) assumed that responses to anthropogenic and natural external forcing are additive. They smoothed the response to anthropogenic forcing using smoothing splines, while leaving the natural forcing response, estimated by an Energy Balance Model (EBM), unsmoothed. The sum of these two components was then used as their forcing response estimate. Li et al. (2025) directly smoothed the ALL forcing response series, thereby implicitly treating the short-term effects of major volcanic eruptions similarly to internal variability. Previous implementations of KCC performed smoothing with splines with knots placed at fixed, arbitrarily chosen points in time that may affect the characterization of smoothed model responses during reference periods. We therefore further built on the approach of Li et al. (2025) by introducing random sampling of different knot placements while enforcing a distance criterion between consecutive knots, which allows us to better characterize the uncertainty of the smoothed model responses during reference periods.

Another way our study differs from many previous studies (e.g., Deser et al., 2020; Y. Li et al., 2025; Qasmi & Ribes, 2022) is that we use only one ensemble member per model to construct the prior distribution. Our rationale is that while the influence of internal variability on forced response estimates can be substantial at the regional scale when based on only single simulations, using only one run per model ensures that the width of the prior reflects the effects of model uncertainty and internal variability in a balanced manner. Reducing this source of uncertainty by unequal amounts for different models would potentially reduce the width of the prior, with models with fewer simulations potentially having a larger influence on its width that models with large numbers of simulations.

Finally, we would be remiss if we did not point out some limitations of the study. In the analysis, we use simulations from 25 climate models to estimate historical warming response to ALL forcing, while the response to other forcings was based on a subset consisting of the 10 models that participated in DAMIP. The ALL forcing estimates from the 25-model ensemble relative to the 1850–2025 are compared with those derived from the 10-model subset in Figure S11 in Supporting Information S1. We found that although both model collections yield similar temperature trends in recent decades, they diverge noticeably during the pre-industrial period. This discrepancy highlights the challenge of estimating warming when the forced response signal is weak, and it directly affects the calculation of attributable warming when using the pre-industrial period as a reference (Figure S12 in Supporting Information S1). It should also be noted that the uncertainty range derived from the 10-model subset is smaller than that from the 25-model set. This is because the 10-model subset describes a narrower prior distribution than the larger 25-model ensemble that in turn affects the width of the posterior distribution. This illustrates a general limitation of the prior ensembles of opportunity and whether they sample adequately from the population of climate models that could, adequately, simulate the system as we have observed it. While inflating the uncertainty range can partially mitigate this issue, more rigorous validation should be pursued in future work.

Appendix A: Implementation of the Observational Constraint Method

The constraint method is applied for estimating historical attributed warming induced by various external forcings, including ALL, ANT, NAT, GHG, OA, as well as future projected warming under different emissions scenarios (SSP1-2.6, SSP2-4.5, SSP3-7.0, SSP5-8.5). To illustrate the implementation, we present three examples of implementations using annual mean temperature averaged over Canada (the CA scheme) that can be generalized to other cases (i.e., SRA and NCG schemes).

A1. Implementation 1: Constraint on the ALL-Forcing Response From 1850 to 2025

1. In this case, $\mathbf{Y}_o$ is a vector of length $n = 76$, representing the annual mean Canadian temperatures from 1948 to 2023, expressed relative to 1961–1990.
2. $\boldsymbol{\mu}$ is a vector of annual mean temperature responses relative to 1961–1990 under ALL forcing during historical period from 1850 to 2025 (length $n = 176$), which is calculated as the mean of single historical ALL forcing simulations from 25 CMIP6 models $\mathbf{X}_i, i = 1, \ldots, 25$. We estimate the forced response by minimizing internal variability through temporal smoothing of the model simulations (see Section 2d). We recognize that by doing so we also smooth out much of climate responses to episodic short-term variations in natural forcing due to large volcanic eruptions.
3. H is constructed to extract the components of $\boldsymbol{\mu}$ that correspond to the observational period. In this case, H has dimensions [76, 176], where 76 is the length of $\mathbf{Y}_o$, and 176 is the length of $\boldsymbol{\mu}$. The matrix is defined as $H = \begin{bmatrix}\mathbf{0} & \boldsymbol{I}_{76} & \mathbf{0}\end{bmatrix}$, where $\boldsymbol{I}_{76}$ is a 76×76 identity matrix placed in the columns corresponding to the years of observation 1948–2023, and the remaining columns are filled with zeros.
4. $\boldsymbol{\Sigma}_o$ characterizes the uncertainty in the observations, which includes internal variability and measurement error. It has dimensions [76, 76] and can be expressed as $\boldsymbol{\Sigma}_o = \boldsymbol{\Sigma}_{iv} + \boldsymbol{\Sigma}_{mea}$. The matrix $\boldsymbol{\Sigma}_{iv}$ is estimated using large ensemble simulations from five climate models, each with more than 30 runs (Table S1 in Supporting Information S1). We assume that the intra-ensemble variability—differences between realizations within a large ensemble—represents the effects of internal variability similarly to that which affects observed values in the real world. The estimation process involves the following steps: (a) For each model, we first calculate residual time series for the period 1948–2023 by subtracting the ensemble mean response for that model from

each individual simulation in the large ensemble. (b) We then use the Ledoit-Wolf (LW) regularized covariance matrix estimator (Ledoit & Wolf, 2004; Ribes et al., 2013) to compute a covariance matrix from these residuals for each model with a large ensemble. (c) The resulting covariance matrices of the five large ensembles are averaged to provide an estimate of $\mathbf{\Sigma}_{iv}$, assuming the exchangeability of internal variability across models. To estimate measurement error $\mathbf{\Sigma}_{mea}$, we use 200 realizations of HadCRUT5, as CanGridT does not provide measurement uncertainty estimates. The variance-covariance matrix $\mathbf{\Sigma}_{mea}$, is estimated as above from these 200 samples to estimate the regional observational uncertainty.

5. $\mathbf{\Sigma}_x$ characterizes model forced response uncertainty. This covariance matrix has size [176, 176] and is derived from the smoothed series from all models $\mathbf{X}_i, i = 1, \ldots, 25$. We treat the available collection of models as a simple random sample of plausible model representations of the Earth system, noting considerable limitations such as model dependence (Knutti, 2010; Tebaldi & Knutti, 2007) and the fact that the available sample represents an ensemble of opportunity (Annan & Hargreaves, 2010; Knutti et al., 2010).

A2. Implementation 2: Constraint on the ANT-Forcing Response From 1850 to 2025

1. The observational series, $\mathbf{Y}_o$, remains the same in Implementation 1.
2. $\boldsymbol{\mu}$ includes two components in this case. The first component is the temperature response over Canada to ALL forcing in the model simulations during the historical period 1948–2023 (spanning 76 years) and the second component is the Canadian temperature response to ANT forcing over the period of 1850–2025 (176 years). Thus, $\boldsymbol{\mu}$ has length $n = 76 + 176 = 252$. The two components of $\boldsymbol{\mu}$ are calculated as the mean of 10 DAMIP ALL forcing simulations (1948–2023) and 10 DAMIP ANT forcing responses (1850–2025) respectively. As noted previously, the ANT forcing responses are obtained by subtracting NAT simulations from ALL simulations. The two components of $\boldsymbol{\mu}$ are centered on the 1961–1990, aligning with the observational series $\mathbf{Y}_o$.
3. Corresponding to the structure of $\boldsymbol{\mu}$, the matrix of H has dimensions [76, 252], where 76 corresponds to the length of $\mathbf{Y}_o$, and 252 to the length of $\boldsymbol{\mu}$. The matrix is defined as $H = \begin{bmatrix} \boldsymbol{I}_{76} & \mathbf{0} \end{bmatrix}$, where $\boldsymbol{I}_{76}$ is a 76×76 identity matrix placed in the first 76 columns, and the remaining columns are filled with zeros.
4. The observational covariance matrix, $\mathbf{\Sigma}_o$, remains the same as in Implementation 1.
5. Corresponding to the structure of $\boldsymbol{\mu}$, covariance matrix $\mathbf{\Sigma}_x$ has dimensions [252, 252] and is calculated from the smoothed ALL and ANT forcing simulations from DAMIP.

Similarly, this approach can be applied to other external forcings (NAT, GHG, OA), maintaining the same structure of each component.

A3. Implementation 3: Constraint on Future Warming Under the SSP2-4.5 Scenario

1. The observational series, $\mathbf{Y}_o$, remains the same as in Implementation 1.
2. As in Implementation 2, $\boldsymbol{\mu}$ is constructed with two components, where the first component remains the same, representing the response to ALL forcing over Canada. The second component is estimated as the mean of historical and future projection simulations for the entire period from 1850 to 2100 (a total of 251 years) by the 25 CMIP6 models under the historical ALL/SSP2-4.5 scenario. Consequently, the size of $\boldsymbol{\mu}$ is $76 + 251 = 327$. As in the other implementations, both components of $\boldsymbol{\mu}$ are centered on the 1961–1990. Note that in this implementation, the first component of $\boldsymbol{\mu}$ is identical to the part of the second component of $\boldsymbol{\mu}$ that represents 1948–2023.
3. Similar to Implementation 2, H is constructed to have dimensions [76, 327] and is defined as $\begin{bmatrix} \boldsymbol{I}_{76} & \mathbf{0} \end{bmatrix}$.
4. The observational covariance matrix, $\mathbf{\Sigma}_o$, remains the same in Implementation 1.
5. Corresponding to the structure of $\boldsymbol{\mu}$, $\mathbf{\Sigma}_x$ has dimensions [327, 327] and is calculated from the smoothed series of the models that provided both historical and future projection experiments.

This approach can similarly be applied to other future emissions scenarios while maintaining the same structure of each component.

Conflict of Interest

The authors declare no conflicts of interest relevant to this study.

Data Availability Statement

The HadCRUT5 data set is available at https://www.metoffice.gov.uk/hadobs/hadcrut5/ (Morice et al., 2021b). The CanGridT mlyV3.1 gridded surface temperature data set is available at https://open.canada.ca/data/en/dataset/781e02cc-6c1b-462e-b61b-f96c607b23bd (Canadian Centre for Climate Services, 2023). The CMIP6 climate model simulations are available via the Earth System Grid Federation at https://esgf-node.ipsl.upmc.fr/projects/cmip6-ipsl/ (Eyring et al., 2016a). The code used to perform the analyses and create the figures is archived on Zenodo (Li, 2025).

Acknowledgments
We thank the World Climate Research Programme's Working Group on Coupled Modelling and the individual modeling groups for their roles in making CMIP data available. Tong Li was supported in part by a grant from Environment and Climate Change Canada.

References

Allen, M. R., & Stott, P. A. (2003). Estimating signal amplitudes in optimal fingerprinting. Part I: Theory. *Climate Dynamics*, *21*(5–6), 477–491. https://doi.org/10.1007/s00382-003-0313-9

AMAP. (2021). Arctic climate change update 2021: Key trends and impacts. Summary for policy-makers. Arctic monitoring and assessment programme (AMAP).

Annan, J. D., & Hargreaves, J. C. (2010). Reliability of the CMIP3 ensemble. *Geophysical Research Letters*, *37*(2). https://doi.org/10.1029/2009GL041994

Bush, E. & Lemmen, D. S. (Eds.) (2019). *Canada's changing climate report*. Government of Canada.

Canadian Centre for Climate Services. (2023). CanGridT mlyV3.1 gridded surface temperature dataset [Dataset]. *Government of Canada*. https://doi.org/10.18164/781e02cc-6c1b-462e-b61b-f96c607b23bd

Cannon, A. J. (2024). The impact of "hot models" on a CMIP6 ensemble used by climate service providers in Canada: Do global constraints lead to appreciable differences in regional projections? *Journal of Climate*, *37*(6), 2141–2154. https://doi.org/10.1175/jcli-d-23-0459.1

Dai, A., Luo, D., Song, M., & Liu, J. (2019). Arctic amplification is caused by sea-ice loss under increasing CO(2). *Nature Communications*, *10*(1), 121. https://doi.org/10.1038/s41467-018-07954-9

Deser, C., Lehner, F., Rodgers, K. B., Ault, T., Delworth, T. L., DiNezio, P. N., et al. (2020). Insights from Earth system model initial-condition large ensembles and future prospects. *Nature Climate Change*, *10*(4), 277–286. https://doi.org/10.1038/s41558-020-0731-2

Douville, H. (2023). Robust and perfectible constraints on human-induced Arctic amplification. *Communications Earth & Environment*, *4*(1), 283. https://doi.org/10.1038/s43247-023-00949-5

Eyring, V., Bony, S., Meehl, G. A., Senior, C. A., Stevens, B., Stouffer, R. J., & Taylor, K. E. (2016a). Overview of the Coupled Model Intercomparison Project Phase 6 (CMIP6) experimental design and organization [Dataset]. *Geoscientific Model Development*, *9*(5), 1937–1958. https://doi.org/10.5194/gmd-9-1937-2016

Eyring, V., Bony, S., Meehl, G. A., Senior, C. A., Stevens, B., Stouffer, R. J., & Taylor, K. E. (2016b). Overview of the Coupled Model Intercomparison Project Phase 6 (CMIP6) experimental design and organization. *Geoscientific Model Development*, *9*(5), 1937–1958. https://doi.org/10.5194/gmd-9-1937-2016

Forster, P. M., Smith, C., Walsh, T., Lamb, W. F., Lamboll, R., Cassou, C., et al. (2025). Indicators of Global Climate Change 2024: Annual update of key indicators of the state of the climate system and human influence. *Earth System Science Data*, *17*(6), 2641–2680. https://doi.org/10.5194/essd-17-2641-2025

Fox-Kemper, B., Hewitt, H. T., Xiao, C., Aðalgeirsdóttir, G., Drijfhout, S. S., Edwards, T. L., et al. (2021). Ocean, cryosphere and sea level change. In V. Masson-Delmotte, P. Zhai, A. Pirani, S. L. Connors, C. Péan, S. Berger, et al. (Eds.), *Climate change 2021: The physical science basis. Contribution of working group I to the sixth assessment report of the intergovernmental panel on climate change* (pp. 1211–1362). Cambridge University Press. https://doi.org/10.1017/9781009157896.011

Gillett, N. P., Kirchmeier-Young, M., Ribes, A., Shiogama, H., Hegerl, G. C., Knutti, R., et al. (2021). Constraining human contributions to observed warming since the pre-industrial period. *Nature Climate Change*, *11*(3), 207–212. https://doi.org/10.1038/s41558-020-00965-9

Gillett, N. P., Shiogama, H., Funke, B., Hegerl, G., Knutti, R., Matthes, K., et al. (2016). The Detection and Attribution Model Intercomparison Project (DAMIP v1.0) contribution to CMIP6. *Geoscientific Model Development*, *9*(10), 3685–3697. https://doi.org/10.5194/gmd-9-3685-2016

Gutjahr, O., Putrasahan, D., Lohmann, K., Jungclaus, J. H., von Storch, J.-S., Brüggemann, N., et al. (2019). Max Planck Institute Earth System Model (MPI-ESM1.2) for the High-Resolution Model Intercomparison Project (HighResMIP). *Geoscientific Model Development*, *12*(7), 3241–3281. https://doi.org/10.5194/gmd-12-3241-2019

Hajima, T., Watanabe, M., Yamamoto, A., Tatebe, H., Noguchi, M. A., Abe, M., et al. (2020). Development of the MIROC-ES2L Earth system model and the evaluation of biogeochemical processes and feedbacks. *Geoscientific Model Development*, *13*(5), 2197–2244. https://doi.org/10.5194/gmd-13-2197-2020

Hjort, J., Streletskiy, D., Doré, G., Wu, Q., Bjella, K., & Luoto, M. (2022). Impacts of permafrost degradation on infrastructure. *Nature Reviews Earth & Environment*, *3*(1), 24–38. https://doi.org/10.1038/s43017-021-00247-8

Kettleborough, J. A., Booth, B. B. B., Stott, P. A., & Allen, M. R. (2007). Estimates of uncertainty in predictions of global mean surface temperature. *Journal of Climate*, *20*(5), 843–855. https://doi.org/10.1175/jcli4012.1

Knutti, R. (2010). The end of model democracy? *Climatic Change*, *102*(3–4), 395–404. https://doi.org/10.1007/s10584-010-9800-2

Knutti, R., Furrer, R., Tebaldi, C., Cermak, J., & Meehl, G. A. (2010). Challenges in combining projections from multiple climate models. *Journal of Climate*, *23*(10), 2739–2758. https://doi.org/10.1175/2009jcli3361.1

Knutti, R., Sedláček, J., Sanderson, B. M., Lorenz, R., Fischer, E. M., & Eyring, V. (2017). A climate model projection weighting scheme accounting for performance and interdependence. *Geophysical Research Letters*, *44*(4), 1909–1918. https://doi.org/10.1002/2016gl072012

Ledoit, O., & Wolf, M. (2004). A well-conditioned estimator for large-dimensional covariance matrices. *Journal of Multivariate Analysis*, *88*(2), 365–411. https://doi.org/10.1016/s0047-259x(03)00096-4

Lee, J. Y., Marotzke, J., Bala, G., Cao, L., Corti, S., Dunne, J. P., et al. (2021). Future global climate: Scenario-based projections and near-term information. In V. Masson-Delmotte, P. Zhai, A. Pirani, S. L. Connors, C. Péan, S. Berger, et al. (Eds.), *Climate change 2021: The physical science basis. Contribution of working group I to the sixth assessment report of the intergovernmental panel on climate change* (pp. 553–672). Cambridge University Press. https://doi.org/10.1017/9781009157896.006

Li, C., Sun, Q., Wang, J., Liang, Y., Zwiers, F. W., Zhang, X., & Li, T. (2024). Constraining projected changes in rare intense precipitation events across global land regions. *Geophysical Research Letters*, *51*(3), e2023GL105605. https://doi.org/10.1029/2023gl105605

Li, G., Zhang, X., Cannon, A. J., Murdock, T., Sobie, S., Zwiers, F., et al. (2018). Indices of Canada's future climate for general and agricultural adaptation applications. *Climatic Change*, *148*(1–2), 249–263. https://doi.org/10.1007/s10584-018-2199-x
Li, T. (2025). Code and figures for "constrained estimates of externally forced past and future warming for Canada" [Software]. *Zenodo*. https://doi.org/10.5281/zenodo.16783209
Li, T., Zwiers, F. W., & Zhang, X. (2025). Should we think of observationally constrained multidecade climate projections as predictions? *Science Advances*, *11*(20), eadt6485. https://doi.org/10.1126/sciadv.adt6485
Liang, Y., Gillett, N. P., & Monahan, A. H. (2020). Climate model projections of 21st century global warming constrained using the observed warming trend. *Geophysical Research Letters*, *47*(12), e2019GL086757. https://doi.org/10.1029/2019gl086757
Min, S.-K., Zhang, X., & Zwiers, F. (2008). Human-induced arctic moistening. *Science*, *320*(5875), 518–520. https://doi.org/10.1126/science.1153468
Min, S.-K., Zhang, X., Zwiers, F., Shiogama, H., Tung, Y.-S., & Wehner, M. (2013). Multimodel detection and attribution of extreme temperature changes. *Journal of Climate*, *26*(19), 7430–7451. https://doi.org/10.1175/jcli-d-12-00551.1
Miner, K. R., Turetsky, M. R., Malina, E., Bartsch, A., Tamminen, J., McGuire, A. D., et al. (2022). Permafrost carbon emissions in a changing Arctic. *Nature Reviews Earth & Environment*, *3*(1), 55–67. https://doi.org/10.1038/s43017-021-00230-3
Morice, C. P., Kennedy, J. J., Rayner, N. A., Winn, J. P., Hogan, E., Killick, R. E., et al. (2021a). An updated assessment of near-surface temperature change from 1850: The HadCRUT5 data set. *Journal of Geophysical Research: Atmospheres*, *126*(3), e2019JD032361. https://doi.org/10.1029/2019jd032361
Morice, C. P., Kennedy, J. J., Rayner, N. A., Winn, J. P., Hogan, E., Killick, R. E., et al. (2021b). An updated assessment of near-surface temperature change from 1850: The HadCRUT5 data set (version 5.0.1.0) [Dataset]. *Met Office Hadley Centre*, *126*(3). e2019JD032361. https://doi.org/10.1029/2019JD032361
Pithan, F., & Mauritsen, T. (2014). Arctic amplification dominated by temperature feedbacks in contemporary climate models. *Nature Geoscience*, *7*(3), 181–184. https://doi.org/10.1038/ngeo2071
Qasmi, S., & Ribes, A. (2022). Reducing uncertainty in local temperature projections. *Science Advances*, *8*(41), eabo6872. https://doi.org/10.1126/sciadv.abo6872
Rantanen, M., Karpechko, A. Y., Lipponen, A., Nordling, K., Hyvärinen, O., Ruosteenoja, K., et al. (2022). The Arctic has warmed nearly four times faster than the globe since 1979. *Communications Earth & Environment*, *3*(1), 168. https://doi.org/10.1038/s43247-022-00498-3
Ribes, A., Boé, J., Qasmi, S., Dubuisson, B., Douville, H., & Terray, L. (2022). An updated assessment of past and future warming over France based on a regional observational constraint. *Earth System Dynamics*, *13*(4), 1397–1415. https://doi.org/10.5194/esd-13-1397-2022
Ribes, A., Planton, S., & Terray, L. (2013). Application of regularised optimal fingerprinting to attribution. Part I: Method, properties and idealised analysis. *Climate Dynamics*, *41*(11–12), 2817–2836. https://doi.org/10.1007/s00382-013-1735-7
Ribes, A., Qasmi, S., & Gillett, N. P. (2021). Making climate projections conditional on historical observations. *Science Advances*, *7*(4), eabc0671. https://doi.org/10.1126/sciadv.abc0671
Screen, J. A., & Simmonds, I. (2010). The central role of diminishing sea ice in recent Arctic temperature amplification. *Nature*, *464*(7293), 1334–1337. https://doi.org/10.1038/nature09051
Sherwood, S. C., Webb, M. J., Annan, J. D., Armour, K. C., Forster, P. M., Hargreaves, J. C., et al. (2020). An assessment of Earth's climate sensitivity using multiple lines of evidence. *Reviews of Geophysics*, *58*(4), e2019RG000678. https://doi.org/10.1029/2019RG000678
Shiogama, H., Tatebe, H., Hayashi, M., Abe, M., Arai, M., Koyama, H., et al. (2023). MIROC6 large ensemble (MIROC6-LE): Experimental design and initial analyses. *Earth System Dynamics*, *14*(6), 1107–1124. https://doi.org/10.5194/esd-14-1107-2023
Shiogama, H., Watanabe, M., Kim, H., & Hirota, N. (2022). Emergent constraints on future precipitation changes. *Nature*, *602*(7898), 612–616. https://doi.org/10.1038/s41586-021-04310-8
Stott, P. A., Kettleborough, J. A., & Allen, M. R. (2006). Uncertainty in continental-scale temperature predictions. *Geophysical Research Letters*, *33*(2), L02708. https://doi.org/10.1029/2005gl024423
Swart, N. C., Cole, J. N. S., Kharin, V. V., Lazare, M., Scinocca, J. F., Gillett, N. P., et al. (2019). The Canadian Earth System Model version 5 (CanESM5.0.3). *Geoscientific Model Development*, *12*(11), 4823–4873. https://doi.org/10.5194/gmd-12-4823-2019
Tebaldi, C., & Knutti, R. (2007). The use of the multi-model ensemble in probabilistic climate projections. *Philosophical transactions. Series A, Mathematical, physical, and engineering sciences*, *365*(1857), 2053–2075. https://doi.org/10.1098/rsta.2007.2076
Tokarska, K. B., Stolpe, M. B., Sippel, S., Fischer, E. M., Smith, C. J., Lehner, F., & Knutti, R. (2020). Past warming trend constrains future warming in CMIP6 models. *Science Advances*, *6*(12), eaaz9549. https://doi.org/10.1126/sciadv.aaz9549
UNFCCC. (2015). Paris agreement. Retrieved from https://unfccc.int/sites/default/files/english_paris_agreement.pdf
Vihma, T. (2014). Effects of arctic sea ice decline on weather and climate: A review. *Surveys in Geophysics*, *35*(5), 1175–1214. https://doi.org/10.1007/s10712-014-9284-0
Vincent, L. A., & Gullett, D. W. (1999). Canadian historical and homogeneous temperature datasets for climate change analyses. *International Journal of Climatology*, *19*(12), 1375–1388. https://doi.org/10.1002/(sici)1097-0088(199910)19:12<1375::Aid-joc427>3.0.Co;2-0
Vincent, L. A., Hartwell, M. M., & Wang, X. L. (2020). A third generation of homogenized temperature for trend analysis and monitoring changes in Canada's climate. *Atmosphere-Ocean*, *58*(3), 173–191. https://doi.org/10.1080/07055900.2020.1765728
Vincent, L. A., Zhang, X., Brown, R. D., Feng, Y., Mekis, E., Milewska, E. J., et al. (2015). Observed trends in Canada's climate and influence of low-frequency variability modes. *Journal of Climate*, *28*(11), 4545–4560. https://doi.org/10.1175/JCLI-D-14-00697.1
Wan, H., Zhang, X., & Zwiers, F. (2018). Human influence on Canadian temperatures. *Climate Dynamics*, *52*(1–2), 479–494. https://doi.org/10.1007/s00382-018-4145-z
Watts, J. D., Potter, S., Rogers, B. M., Virkkala, A. M., Fiske, G., Arndt, K. A., et al. (2025). Regional hotspots of change in northern high latitudes informed by observations from space. *Geophysical Research Letters*, *52*(2), e2023GL108081. https://doi.org/10.1029/2023gl108081
WMO. (2023). State of the global climate 2023.
Zeke Hausfather, K. M., Schmidt, G. A., Nielsen-Gammon, J. W., Mark, Z., & Zelinka, M. (2022). Climate simulations: Recognize the 'hot model' problem. *Nature*, *605*(7908), 26–29. https://doi.org/10.1038/d41586-022-01192-2
Zhang, X., Flato, G., Kirchmeier-Young, M., Vincent, L., Wan, H., Wang, X., et al. (2019). Changes in temperature and precipitation across Canada: Chapter 4. In E. Bush & D. S. Lemmen (Eds.) *Canada's changing climate report* (pp. 112–193).
Zhang, X., Vincent, L. A., Hogg, W. D., & Niitsoo, A. (2000). Temperature and precipitation trends in Canada during the 20th century. *Atmosphere-Ocean*, *38*(3), 395–429. https://doi.org/10.1080/07055900.2000.9649654
Ziehn, T., Chamberlain, M. A., Law, R. M., Lenton, A., Bodman, R. W., Dix, M., et al. (2020). The Australian Earth system model: ACCESS-ESM1.5. *Journal of Southern Hemisphere Earth Systems Science*, *70*(1), 193–214. https://doi.org/10.1071/ES19035